Appendix A

Altitude of Saturn's aurora

A.1 Forewords

Most of the techniques developed to study the Io footprint on HST images can and have been extended to other studies based on the same type of images. We noted in Chapter 2 that the scripts used to generate the Jupiter HST imaging and spectral database and catalog have been adapted to build similar Saturn HST imaging database and catalog. The analysis of Saturn images demonstrates that radial cuts inflection points can be used to reliably and automatically compute the planetary center position on the HST images. Similarly, the methods developed to study the Io footprint tail vertical profiles can also be applied to Saturn's auroral emissions. The present appendix presents a peper in which we used the limb-scanning technique developed for the Io tail emissions to study the altitude of Saturn's aurora. The main difference is that, in the present case, we cannot be sure that the emission region is exactly in the limb plane. Actually, the measured peak altitude represents the minimum value for the real peak altitude for geometrical reasons: if the emission region is not located exactly in the limb plane, its apparent altitude is smaller than its real altitude (see Figure A.1). If the UV light hydrocarbon absorption were strong, the opposite effect, i.e. an over-estimation of the actual peak altitude, would take place. No short wavelength light could escape from the atmosphere from below the hydrocarbon homopause, setting an apparent peak altitude threshold. However, this latter effect is very unlikely to affect our images since UV spectra usually show little or no FUV absorption signature (see the discussion in the next section).

The estimate of the peak auroral altitude, together with measurements of the emission region pressure and temperature, led us to modify the equatorial atmo-

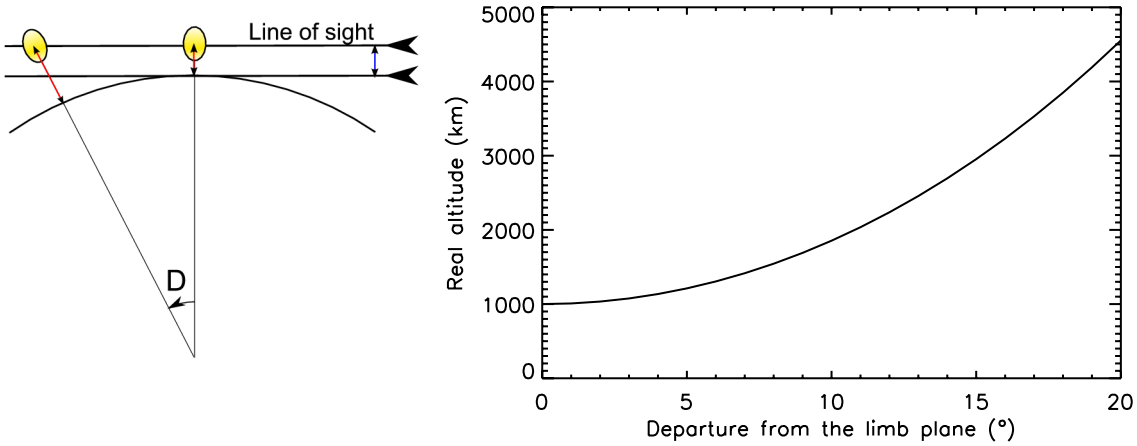

Figure A.1: (right) Evolution of the real emission altitude as a function of the angular distance (D) from the limb plane. The observed emission altitude is set at 1000 km.

spheric model in order to meet the observational constraints in the polar regions. Additional details on the way this model is built are given in Section A.3. Finally, in the last section of this appendix, I describe how the routines that I developed to derive the precipitating electron energy distribution in the Io footprint tail were applied to characterize the energy distribution leading to the Kronian main auroral emissions.

A.2 Publication: Altitude of Saturn's aurora and its implications for the characteristic energy of precipitated electrons

J.-C. Gérard, B. Bonfond, J. Gustin, D. Grodent

Laboratoire de Physique Atmosphérique et Planétaire, Université de Liège, Liege, Belgium

J. T. Clarke

Center for Space Physics, Boston University, Boston, Massachusetts, USA

D. Bisikalo, V. Shematovich

Insitute of Astronomy, Moscow, Russia

Published in the January 2009 issues of Geophysical Research Letters (*Gérard et al.*, 2009).

A.2.1 Abstract

Images of Saturn's aurora at the limb have been collected with the Advanced Camera for Surveys on board the Hubble Space Telescope. They show that the peak of Saturn's nightside emission is generally located 900– 1300 km above the 1-bar level. On the other hand, methane and H_2 columns overlying the aurora have been determined from the analysis of FUV and EUV spectra, respectively. Using a low-latitude model, these columns place the emission layer at or above 610 km. One possibility to solve this apparent discrepancy between imaging and spectral observations is to assume that the thermospheric temperature in the auroral region sharply increases at a higher pressure level than in the low-latitude regions. Using an electron transport code, we estimate the characteristic energy of the precipitated electrons derived from these observations to be in the range 1–5 keV using a low latitude model and 5–30 keV in case of the modified model.

A.2.2 Introduction

Images collected with the Hubble Space Telescope (HST) have shown that Saturn's auroral morphology is characterized by a dynamic aurora ring located between 70° and 80° which responds to the solar wind dynamic pressure (*Gérard et al.* (2004); *Clarke et al.* (2005); *Grodent et al.* (2005a)). The energy of the primary auroral electrons exciting the H2 emissions in Saturn's ultraviolet aurora has so far only been determined indirectly using two distinct spectral methods. The first approach makes use of the FUV color ratio, taking advantage of the strong wavelength dependence of the methane absorption cross section between 130 and 145 nm. When the emission layer is located below the homopause, the altitude where the molecular and eddy diffusion coefficients are equal, wavelengths <145 nm are partly absorbed by the overlying hydrocarbon column. Ultraviolet spectra of Saturn's aurora at ∼3 nm resolution were first obtained with the UVS instrument during the Voyager 1 and 2 flybys of the planet (*Broadfoot et al.* (1981); *Sandel et al.* (1982)). *Broadfoot et al. (1981)* noted that limb scans with the UVS slit locate the auroral emission approximately 800 km above the limb. *Sandel et al.* (1982) found that, unlike the Jovian aurora, most spectra of Saturn's aurora did not indicate the presence of absorption by hydrocarbons. A particularly bright spectrum was best fitted with a CH_4 column of 8×10^{15} cm^{-2}, suggesting an electron energy of ∼10 keV. Six auroral spectra obtained with the Space Telescope Imaging Spectrograph (STIS) were analyzed by *Gérard et al.* (2004) who found indications of a weak absorption by methane. Using *Moses et al. (2000)* low latitude atmosphere model and an electron energy – H_2 column relationship, they derived a primary electron energy of 12 ± 3 keV. Recently, *Gustin et al.* (2009) analyzed a Cassini-UVIS FUV spectrum moderately absorbed by a vertical CH_4 column of 1.2×10^{16} cm^{-2}, corresponding to electron energies near ∼10 keV. Other UVIS spectra were found to be unabsorbed by methane (J. Gustin, private communication, 2008), suggesting that the maximum electron energy is ∼15 keV, which corresponds to an altitude of ∼620 km in the low-latitude atmospheric model by *Moses et al. (2000)*. A second approach is based on the presence of self-absorption of H_2 lines below 120 nm. Transitions connecting to the ground state $v'' = 0$ and 1 vibrational level may be self-absorbed by the overlying H_2 gas, leading to a weakening of EUV specific lines and an increase of intensities at longer wavelengths (*Gustin et al.* (2004a)). *Sandel et al.* (1982) found that one UVS spectrum was best fitted using a spectral model with an overlying H_2 column of 1×10^{20} cm^{-2}. *Gustin et al.* (2009) used a detailed spectral model

to make a thorough analysis of spectra at ∼0.2 resolution collected with the Far Ultraviolet Spectroscopic Explorer (FUSE) satellite. An excellent fit to the line intensity distribution found a rotational temperature of ∼400 K, in agreement with the 420 ± 50 K obtained by *Melin et al.* (2007) from ground based H_3^+ IR spectra. A foreground vertical H_2 abundance of 3×10^{19} cm^{-2} derived from the FUSE spectra corresponds to a pressure level of ∼0.1 µbar, independently of any atmospheric model, and to an altitude of ∼660 km in the *Moses et al.* (2000) model.

A.2.3 Observations and Data Analysis

The HST FUV images used for this study were taken during the HST-Cassini campaign (GO 10862 program) between January 13, 2007 and February 16, 2008 when the subsolar latitude ranged from 14.2° S to 8.3° S. They were obtained with the photon-counting Multi-Anode Micro-channel Array (MAMA) of the High Resolution Camera Solar Blind Channel (SBC) on the Advanced Camera for Surveys (ACS). The point spread function is <2 pixels FWHM. Images were taken both with the F125LP filter (sensitive to the H_2 Lyman and Werner bands but excluding the H Lyman–α line) and with the F115LP filter (which includes Lyman–α). In this program, a typical orbit sequence consists of five 100-s exposures taken with the F125LP filter (Ly-α rejected), followed by nine 100-s exposures with the F115LP filter (Ly-α included) and finally another five 100-s exposures with the F125LP filter. The field of view of 35×31 arcsec^2 is wider than Saturn's apparent equatorial diameter of 10 arcsec, and thus also includes part of the ring system of the planet.

After dark current subtraction and flat-field and geometric corrections, the final image plate scale is 0.0301 arcsec/pixel in each direction. The first step in the analysis consists in the accurate determination of the planetary center. Since the HST pointing accuracy is limited by the onboard guide star catalogue that may include a 1-arcsec (∼30 pixels) uncertainty, the planetary central pixel must be determined using the image itself. Given the Earth-Saturn distance for the time of the observation and the plate scale, our automatic method fits elliptic ribbons to the Kronian A, B and C rings. The center of these ellipses provides an estimate of Saturn's center position in the field of view of ACS with an accuracy of ∼1 pixel. The plate scale is then directly converted into an altitude scale so that the location of the 1-bar level may be determined. To improve the signal to noise ratio, images have been co-added by sets of 5 consecutive images obtained with the same filter.

Radial cuts of the planetary disk at different angles are then generated and are rebinned to increase the signal to noise ratio.

Figure A.9 shows an example of an ACS exposure obtained on January 21, 2007 at 0322 UT with the F115LP filter clearly showing a brightness gap between the limb and the auroral emission. The altitude of the 1-bar level calculated from the camera plate scale is indicated by the white contour. It is seen that this contour agrees within one pixel with the position of the observed sunlit limb, corresponding to the 1-bar altitude level. Figure A.9 also shows the observed light curve along a radial cut through the auroral region. The location of the calculated 1-bar level altitude is shown by the vertical dashed line. The brightness decreases rapidly above the limb but increases again beyond 650 km. The light curve shows a peak near 1150 km, corresponding to the auroral emission layer observed on the image of the planetary disk.

A.2.4 Altitude of the Auroral Emission Peak

To analyze the dataset, an automatic algorithm performs radial scans from the planet's center with 0.1° steps to cover the entire southern auroral region. For each step, the algorithm determines the maximum in the light curve between 0 and 2000 km. A median filtering over 20 profiles (i.e. ∼2°) is then performed and the code identifies the longest sequence of points above 500 km. This sequence retains only the points where the light curve gap is observed under the auroral emission. We then compute the maximum peak altitude in this point sequence with the median filter. This method provides the actual altitude of the emission layer assuming that the aurora is located in the plane of the observed planetary limb and provides a lower limit otherwise. Our statistical study is based on 836 individual images leading to 176 light curves. We find that the average emission peak is 1111 ± 347 km for exposures taken with the F115LP filter, 1181 ± 251 km with the F125LP filter, leading to an average value of 1145 ± 305 km when all images are considered. The 70 km difference between the two filters is not significant, considering the value of the standard deviations.

We now examine the implications of this altitude determination and how they fit with the other constraints based on analysis of FUV and EUV spectra. To summarize, the FUSE spectra indicate that the auroral emission originates from a level of ∼0.1 µbar in a region where the temperature is ∼400 K, a value incompatible

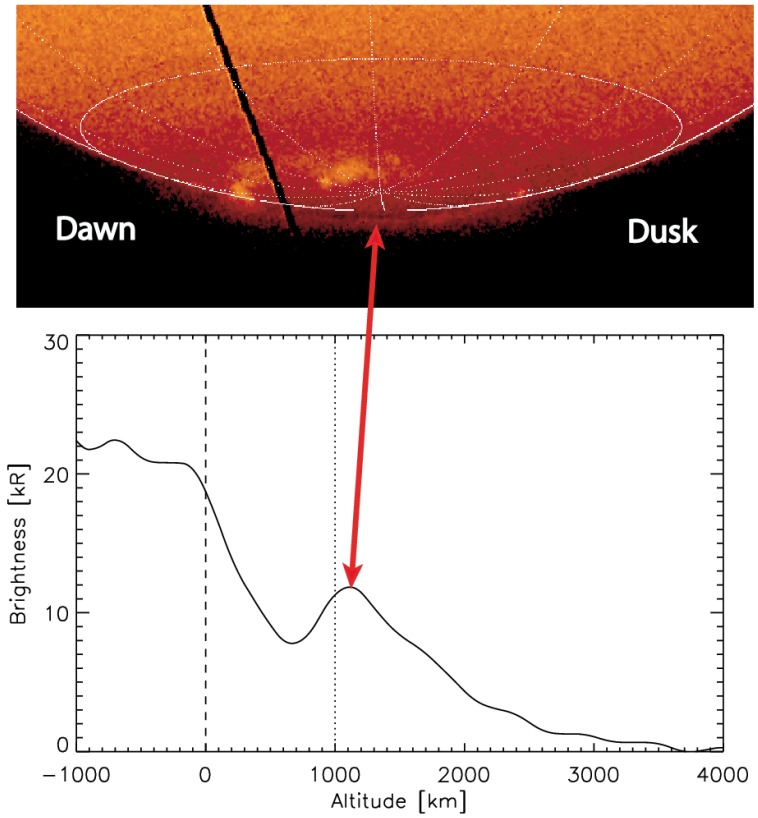

Figure A.2: (top) Zoom on an image of Saturn's south polar region obtained with the ACS camera. Auroral emission is clearly observed beyond the nightside limb. The white contours indicate the calculated location of the 1-bar level; parallels and meridians are shown 30° apart. The dark oblique stripe is the shadow of the detector repelling wire of the ACS camera. The dashed and the dotted lines indicate the 0 and 1000 km respectively. (bottom) Cut through the auroral region showing an emission peak near 1150 km.

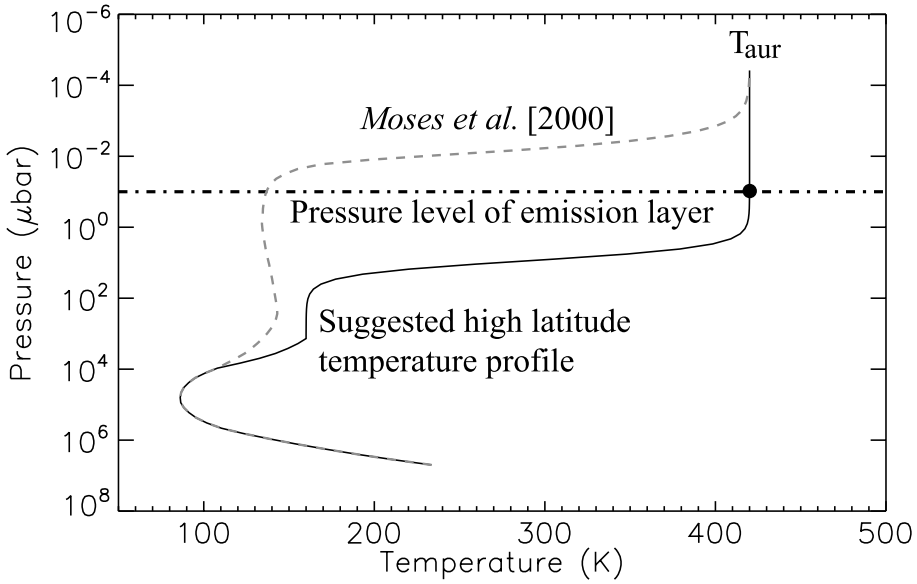

Figure A.3: Pressure-temperature relationship in the *Moses et al.* (2000) model transposed to polar latitudes (dashed line) and in an alternative possible high-latitude model (solid line). The horizontal line indicates the 0.1 μbar level and the full circle indicates the temperature at this pressure level.

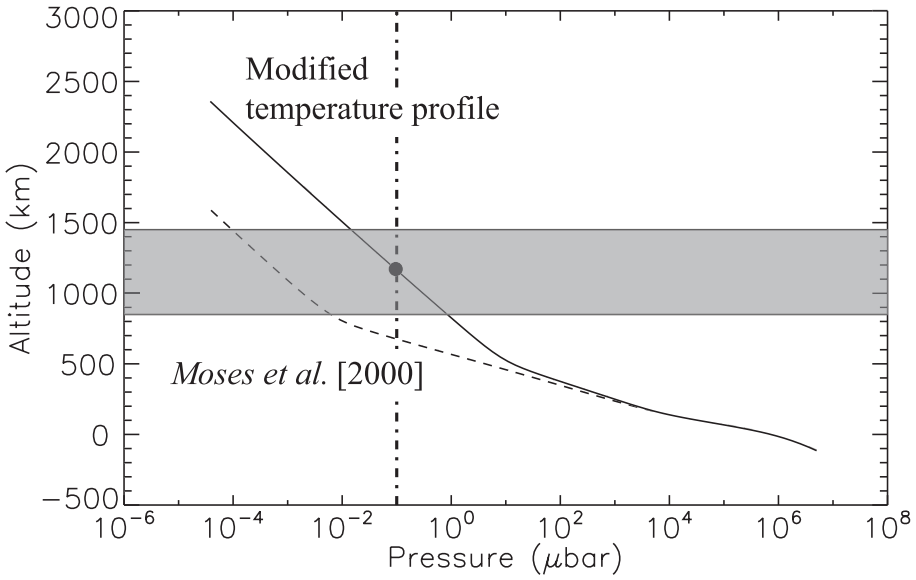

Figure A.4: Altitude-pressure relationship in the *Moses et al.* (2000) model adapted to polar latitudes (dashed line) and in the modified model (solid line). The vertical line indicates the 0.1 μbar level deduced from spectral constraints and the grey zone shows the range of peak altitudes derived from the present study. The full circle indicates the region meeting the pressure and altitude observational constraints.

with 135 K at 0.1 µbar provided by the low-latitude model of *Moses et al.* (2000). Figure A.3 compares observational results with the pressure-temperature relationship in the low-latitude model by *Moses et al.* (2000) adapted to auroral latitudes by adjusting the value of the gravity. The 0.1-µbar pressure determined from the FUSE spectra is indicated by a horizontal line and the auroral temperature of 400 K derived from the H_3^+ and the H_2 spectra is indicated by a closed circle. Another disagreement between auroral observations and the Moses et al. model is clearly apparent in Figure A.4 showing the altitude-pressure relationship. The vertical lines at 0.1 µbar show the emission level based on the FUSE spectra and the horizontal bars define the range of variability of the auroral emission peak centered on 1150 km. The circle locates the central point meeting both constraints. It is situated at a pressure level approximately two orders of magnitude larger than the *Moses et al.* (2000) model at 1150 km. Inversely, in the Moses et al. model, the 0.1 µbar pressure is at an altitude of ∼600 km, 550 km below our auroral limb observations. We thus conclude that the low latitude model cannot match the observational evidence derived from a recent set of auroral spectral observations. In particular, Figure A.3 shows that the strong evidence (from both IR and FUV spectra) of an auroral tem-

perature of ∼400 K is met at pressures less than 2×10^{-2} µbar. To reconcile both datasets, we speculate that the thermal structure of the auroral upper atmosphere of Saturn is modified by the presence of auroral particle and Joule heating whose effect is to deposit energy and heat up the region located below the 10^{-2} µbar level. This heating does not appreciably increase the local exospheric temperature since meridional transport efficiently redistributes heat from the polar to the equatorial regions. The role of transport was demonstrated by *Smith et al.* (2005) using a three-dimensional atmospheric circulation model. As an example, Figure A.3 presents an alternative model meeting the observational constraints listed before. We arbitrarily modified the temperature between 10^3 and 10^{-4} µbar in such a manner as to reach a value of ∼400 K at the 0.1 µbar level. The functional dependence used by *Yelle et al.* (1996) for Jupiter's thermosphere is adopted with a mesospheric temperature $T_0 = 160$ K, an α parameter = 0.03, and an exospheric temperature $T_\infty = 420$ K reached at $z_m = 650$ km. Between 1 and 10 mbars, the temperature profile is a linear combination between *Moses et al.* (2000) values and the expression given by *Yelle et al.* (1996). From this modified pressure-temperature relationship, the new pressure-altitude curve is derived assuming hydrostatic equilibrium and shown in Figure 3. Incidentally, we note that the faster increase of temperature above the 1-bar level probably implies a lowering of the altitude of the homopause compared to the low latitude value. In this case, the full circle corresponding to a pressure of 0.1 µbar and an altitude of 1150 km falls near the center of the rectangle defined by the observational constraints from the FUSE spectra and the HST limb images, while meeting the 400 K determination from the EUV and infrared auroral spectra.

We now examine what may be inferred from the altitude of the emission layer about the characteristic energy of the auroral electrons. For this purpose, a series of simulations has been made with an electron transport code to calculate the vertical distribution of the H_2 FUV volume emission rate. These calculations are based on a direct simulation Monte Carlo method solving the Boltzmann equation described by *Shematovich et al.* (1994) for the Earth's thermosphere. It was subsequently applied by *Bisikalo et al.* (1996) to an H_2-dominated upper atmosphere by replacing cross sections by those appropriate to proton and electron collisions with H_2 and H. Figure A.5 illustrates the altitude distribution of the total H_2 Lyman and Werner band emission calculated for a series of monoenergetic electron beams ranging from ∼750 eV to 30 keV with an isotropic pitch angle distribution. The dashed line curves have been obtained using the *Moses et al.* (2000) model adapted to gravity in the

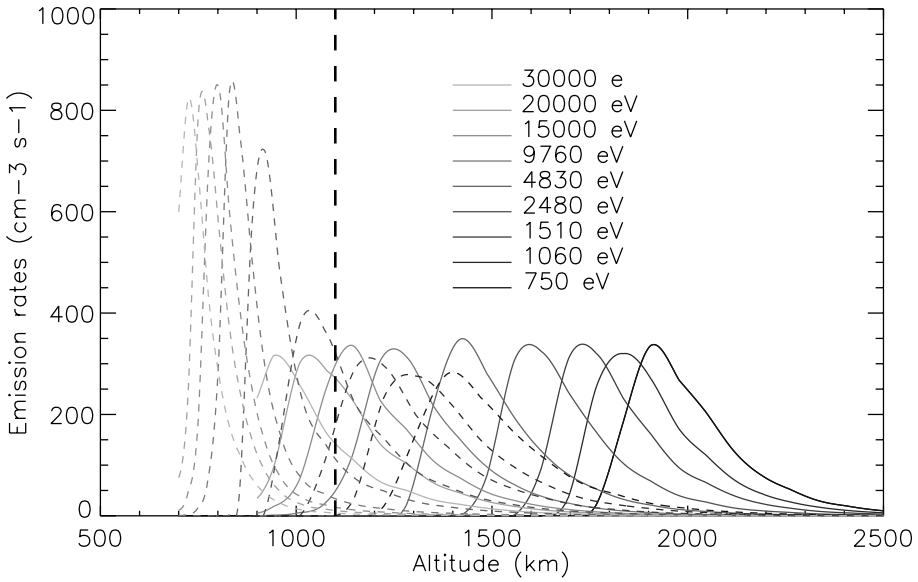

Figure A.5: Volume emission rate of H_2 FUV emissions calculated with a Monte Carlo electron transport code for various primary electron energies. Dotted lines, the low latitude model by *Moses et al.* (2000) is used; solid lines, same using the modified temperature profile model shown in Figure A.3.

polar regions. To generate an emission peak at 1100 km, simulations show that electron energies need to be about 2 keV. This value is close to the that obtained in recent models (*Cowley et al.* (2008), and references therein) as the minimum field-aligned voltage required to produce the current density compatible with Cassini observations.

The simulations also show that electrons about 20 keV are required to generate an emission peak at 0.1 µbar, independently of the temperature profile. The consequence is that in order to produce auroral emission at 1100 km, the pressure levels must be located at a higher altitude than in the low-latitude model. For comparison, calculations performed with the modified model are illustrated in Figure 4 by the solid lines. As expected, all curves for a given energy are now located at a higher altitude. In particular, electrons with energies of about 20 keV produce an emission peak at 1100 km, the auroral altitude determined in this study.

We also note that this result depends somewhat on the adopted pitch angle distribution. For example, if the precipitation is field-aligned, the pressure reached by 20 keV electrons would be less than doubled, changing from 0.06 to 0.1 µbar. In other words, the energy required for field aligned electrons to reach a given pressure

level would be approximately divided by 2, corresponding to an energy of ∼10 keV.

A.2.5 Conclusions

Analysis of over 800 images of Saturn's FUV aurora above the nightside limb indicate that the maximum H_2 emission is observed at an altitude of about 1100 km. A set of independent spectral observations indicate that i) the temperature prevailing in the region of emission is close to 400 K, ii) the auroral electron energy is occasionally high enough to produce a weak absorption by methane, iii) the H_2 column overlying the emission layer corresponds to a pressure level of about 0.1 µbar. Electrons of 15–20 keV deposit their energy at this pressure level, independently of the detailed thermal structure. We find that the set of different observations can only be reconciled if the thermal structure of the high-latitude thermosphere is different from the low-latitude reference model available so far.We estimate the characteristic energy of the precipitating electrons giving a luminosity peak near 1100 km to be in the range 1–5 keV using a low latitude model and 5–30 keV in case of the modified model.

The occasional presence of hydrocarbon absorption in the FUV spectra may result from sporadic hardening of the energy spectrum of the precipitated electrons. The results of our numerical simulations in Figure A.5 indicate that >10 keV electrons may produce emission near the homopause region located at ∼800 km in the low-latitude model. However, ∼100 keV electrons would be needed in our modified profile, in which the homopause altitude is close to 500 km, in order to generate a significant absorption in the FUV. Further study of the circumstances when hydrocarbon absorption is observed should help to clarify this issue.

A.3 Additional details on the modified Kronian polar atmospheric model

In the above section, we highlighted the danger to extrapolate atmospheric models constrained by equatorial measurements to the polar regions. We already discussed this issue on Section 5.5 when we tried to reconcile direct altitude measurement and color ratio measurements for the IFP tail. On Saturn, we proposed a modified model for the polar region atmospheric vertical profiles on Saturn. Here I provide more details on how this modified atmosphere is built and some underlying consequences.

The modified model is basically an empirical modification of the equatorial atmosphere model from *Moses et al.* (2000) (hereafter called Moses model) designed to meet three observational constrains: the pressure (∼0.1µbar), the temperature (∼ 400 K) and the altitude (∼1100 km) of the auroral emissions. The pressure-temperature profile we adopted is divided into three parts:

- for pressures bellow $10^3\mu$bar, the temperature is described by the following formula (from *Yelle et al.* (1996)):

$$T(a) = T_0 + \frac{T_\infty - T_0}{1 + e^{-\alpha(a-a_m)}}$$

  where a is the altitude of the considered point[1] (in km), T_0 is the mesospheric temperature (in K), T_∞ is the exospheric temperature (in K), α is linked to the maximum temperature gradient [2] and a_m is the maximum gradient altitude (in km). The adopted values are: $T_0 = 160$K, $T_\infty = 420$K, $\alpha = 0.04$ and $a_m = 550$ km.

- for pressures above $10^4\mu$bar, the pressure temperature relationship is identical to the one from the Moses model,

- between $10^3\mu$bar and $10^4\mu$bar, the temperature profile is a linear combination transition between the 2 above profiles.

Starting from our new pressure-temperature relationship, we computed the altitude profile as a function of the pressure, based on the hydrostatic equilibrium formula:

$$z_1 = z_0 - (p_1 - p_0)\frac{kT_1}{M_1 g_1}$$

where k is the Boltzmann constant[3] and z_x is the altitude (in m), p_x is the pressure (in Pa), T_x is the temperature (in K), M_x is the mean molecular mass (in kg) and g_x is the gravity acceleration (in m/s) at level x. Note that the gravity acceleration is evaluated for each step assuming a latitude of 80°. The mean molecular mass is also re-evaluated for each step based on the pressure-composition profiles from the Moses model. It can be seen in Figure A.4 that this new profile meets the

[1] At this stage, the altitude-pressure relationship is still the one from the Moses model. We will only adapt this relationship later in the process.

[2] $\alpha = \frac{4}{T_\infty - T_0}\frac{dT}{dz}|_{z=z_m}$ where z_m is the altitude of maximum temperature gradient.

[3] $k = 1.3807 \times 10^{-23}$J/s.

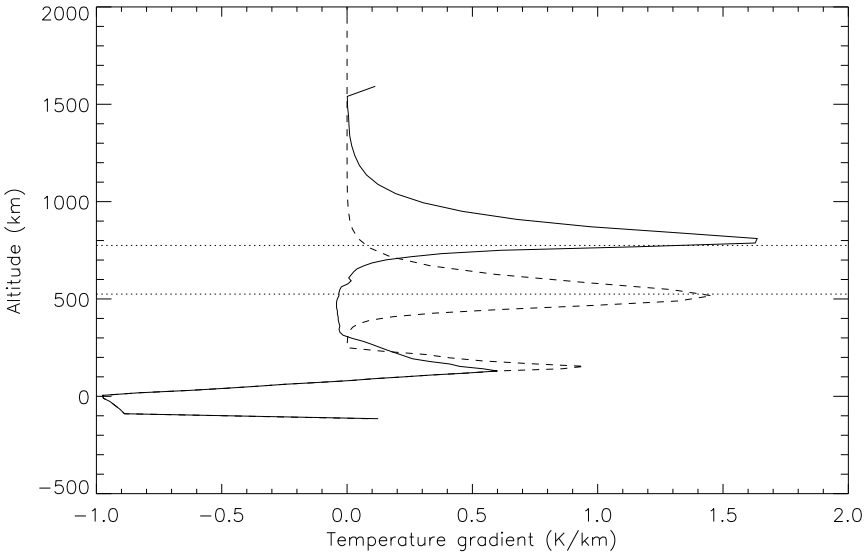

Figure A.6: Plot of the vertical temperature gradient. The solid line corresponds to the Moses model and the dashed line represents the modified profile.

observational constraints while the Moses profile, even adapted for the gravity a 80° latitude does not.

Figure A.6 shows that the new temperature-pressure relationship keeps approximately the same maximum temperature gradient value, but this maximum is shifted from 800 km to 500 km.

The density profile is then computed from the perfect gas law:

$$n = \frac{p}{kT}$$

where n is the density, p is the pressure, k is the Boltzmann constant and T is the temperature. Figure A.7 shows the original Moses density profile (i.e. for a 30° latitude) in dotted line, the Moses profile adapted for the gravity at 80° latitude in solid line and the new modified profile in dashed line.

The modifications we propose to make the polar atmosphere model compatible with measurements is purely ad-hoc and empirical. However, the fact that the temperature raises deeper than in the equatorial regions has physical causes. Usually,

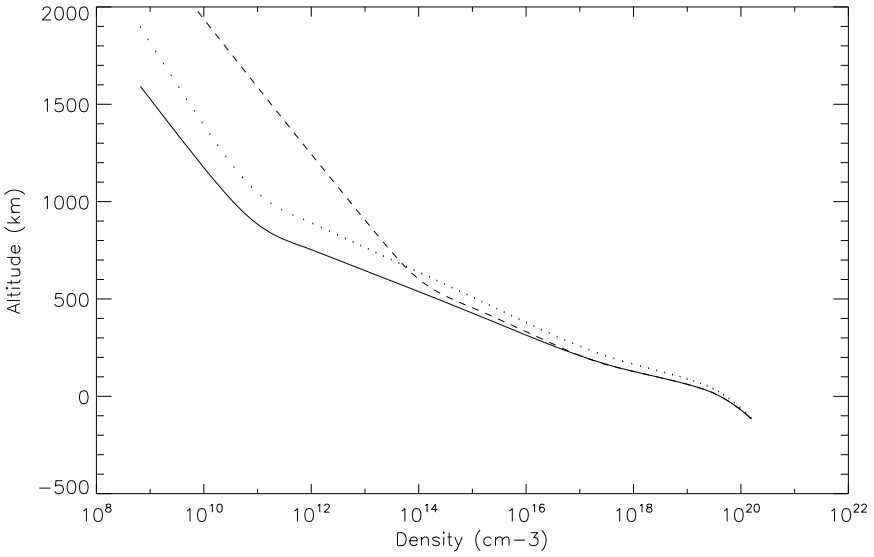

Figure A.7: Density profiles. The solid line represents the profile from the equatorial Moses model adapted for 80° latitude. The dotted line line represents the original Moses profile at 30° latitude. The dashed line represents the output of the new modified model.

the region where the temperature abruptly increases in giant planet atmospheres corresponds to the hydrocarbon homopause. Indeed these molecules generally act as a cooler for the atmosphere, radiating the excess energy to space in the form of IR emissions. The hydrocarbon content of the atmosphere sharply decreases when turbulent diffusion is not sufficient to homogenize the atmospheric constituents. The dominant hydrocarbon molecule in the giant planets atmospheres is methane (CH_4). The methane homopause is defined as the point where the molecular and eddy diffusion coefficients for methane are equal. The changes we propose for the temperature profile, and therefore, to the density profile also affect the molecular diffusion coefficient. This coefficient can be computed with the following formula (*Gladstone*, 1982):

$$D(z) = 2.3 \times 10^{17} \frac{T(z)^{0.765}}{n(z)} \sqrt{\frac{16.04}{m} \frac{m + 2.016}{18.059}}$$

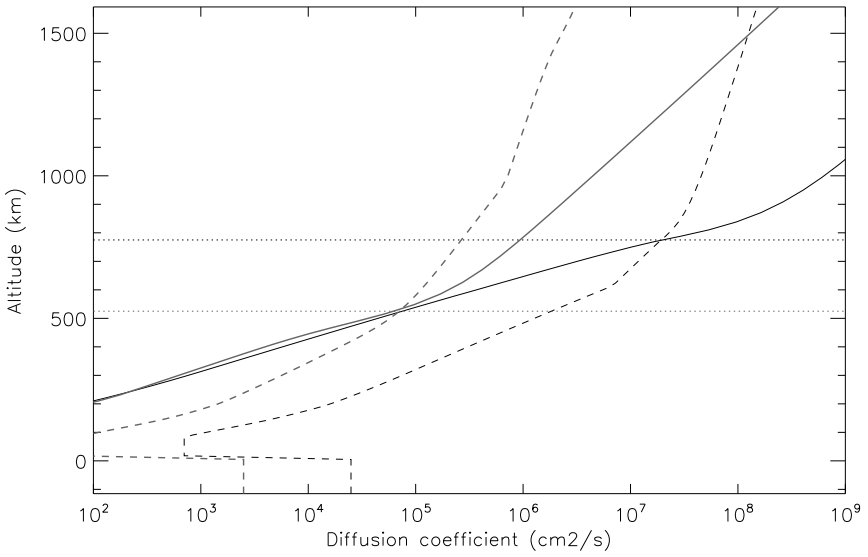

Figure A.8: Profiles of the diffusion coefficients as a function of the altitude. The black lines correspond to the Moses model while the red lines correspond to the modified atmosphere. The molecular diffusion coefficients are show on solid lines and the eddy diffusion coefficients are shown in dashed lines.

where m is the CH_4 molecular mass ($m_{CH_4} = 16$),$D(z)$ is the molecular diffusion coefficient in cm^2s^{-1}, $T(z)$ is the temperature in K and $n(z)$ is the total density in cm^{-3}. Figure A.8 shows the molecular diffusion coefficients both from the Moses model and the modified model. The eddy diffusion coefficient is much more complex and poorly constrained. We chose here to keep the relationship between eddy diffusion coefficient and the pressure from the Moses model. We determine that we need to divide the eddy diffusion coefficient by a factor of 15 to get an homopause altitude corresponding to the new temperature gradient altitude.

A.4 Estimate of the particle energy distribution

Since we are able to extract vertical profiles of Saturn's auroral emissions, it is also possible to remove an empirical background disk intensity profile in order to obtain

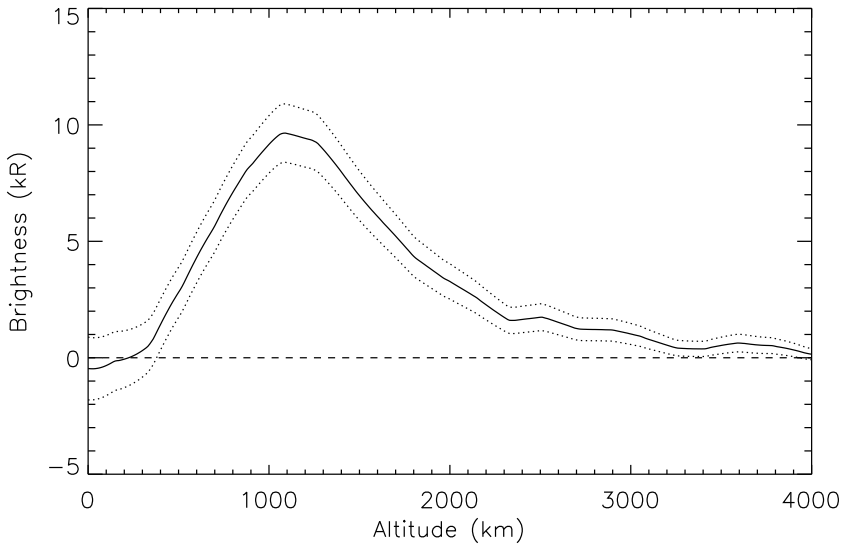

Figure A.9: Example of radial profile through the Kronian aurora. An empirical background disk profile has been removed.

a vertical profile only containing the auroral contribution (Figure A.9). On the case of Saturn, the disk profile is simply a radial profile extracted outside of the auroral region. We note that by removing the disk background, the mean peak altitude decreased down to 1050 km (which remains within the uncertainty bars of the previous estimate). Moreover, if we try to fit a Chapman profile (see Equation 5.1) to the observed curve, as we did for the Io tail, the emission scale height is 550 ± 115 km.

We can now try to find the theoretical electron energy distribution that matches the observed profile, as we did for tail profiles on Jupiter. Assuming a mono-energetic, a Maxwellian or a Kappa distribution, we seek for the set of parameters that best fits the observed profile (Figure A.10). The corresponding differential intensities are shown in Figure A.11. The mean energies deduced from the best fits range from $\sim$10 keV for the Kappa distribution to $\sim$20 keV for the mono-energetic one, the mean energy for the Maxwellian distribution being around $\sim$12 keV. Similarly to the Io tail profiles, the Kronian profile width can neither be reproduced satisfactorily with a mono-energetic distribution nor by a Maxwellian distribution. However, even the Kappa distribution seems unable to reproduce the high altitude part of the profile. Consequently, the energy spectrum of these three theoretical

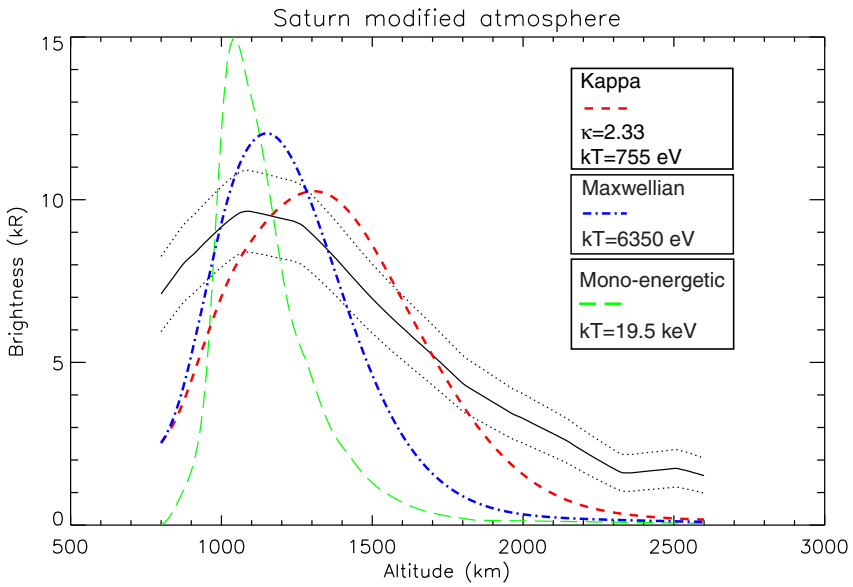

Figure A.10: Observed and simulated vertical emission profiles. The observations and the estimated uncertainties are represented by the solid line surrounded by the dotted lines. The three other lines are the best fit vertical profiles based the theoretical distributions. The green long dashed line corresponds to the mono-energetic distribution, the red small dashed line to the kappa distribution and the blue the dash-dotted line to the Maxwellian distribution. None of these theoretical profiles provides a reasonable fit of the observed curve because they underestimate the high altitude emissions.

distributions is too narrow and a soft energy component appears to be missing.

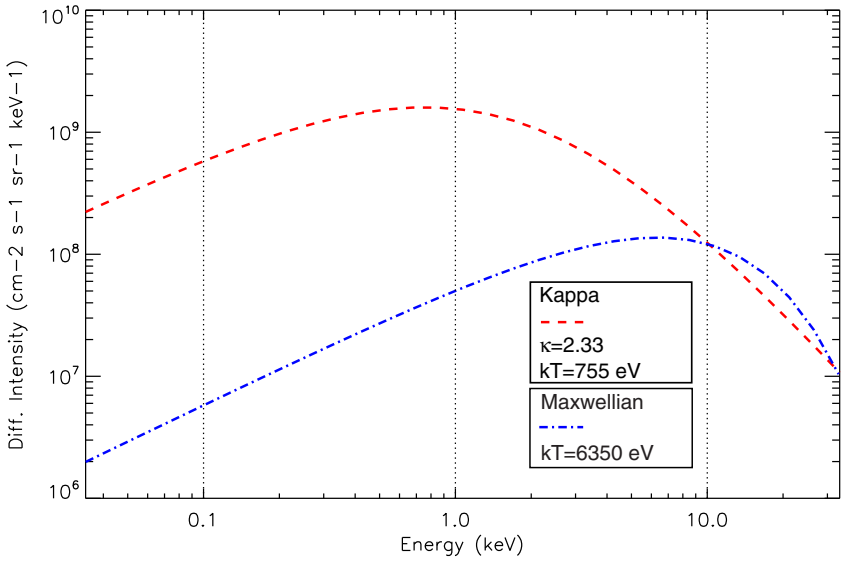

Figure A.11: Energy spectra computed with the best fit parameters for a kappa distribution (red dashed line), and a Maxwelllian distribution (blue dash-dotted line). Note that these intensities are computed assuming an auroral curtain width of 1000 km. This implies that if the real width of the curtain is 500 km, these values should be multiplied by a factor of 2.